RESEARCH ARTICLE

ADVANCED FUNCTIONAL MATERIALS
www.afm-journal.de

On the Electrochemical Activation of Nanoporous Reduced Graphene Oxide Electrodes Studied by In Situ/Operando Electrochemical Techniques

María del Pilar Bernicola, Mailis Lounasvuori, Jessica Padilla-Pantoja, Jose Santiso, Catherine Debiemme-Chouvy, Hubert Perrot, Tristan Petit, Jose A. Garrido, and Elena del Corro**

Due to the difficult access of the electrolyte into the nanoconfined space of nanoporous reduced graphene oxide (rGO) electrodes, achieving the optimal electrochemical performance of these devices becomes a challenge. In this work, the dynamics of interfacial-governed phenomena are investigated during a voltage-controlled electrochemical activation of nanoporous rGO electrodes that leads to an enhanced electrochemical performance in terms of areal capacitance and electrochemical impedance. In situ/operando characterization techniques are used to reveal the dynamics of the irreversible material changes introduced during the activation process, including ionic diffusion and water confinement within the nanopores, along with the reduction of oxygenated groups and the decrease of the rGO interlayer distance. Furthermore, operando techniques are used to uncover the origin of the complex polarization-dependent dynamic response of rGO electrodes. The study reveals that the reversible protonation/deprotonation of remaining functional groups and the cation electro-adsorption/desorption process in the graphene basal plane govern the pseudocapacitive performance of nanoporous rGO electrodes. This work brings new understanding of the complex interplay between surface chemistry, ion confinement, and desolvation processes occurring during electrochemical cycling in nanoporous rGO electrodes, offering new insights for designing high-performing electrodes based on nanoporous rGO.

1. Introduction

Nanoporous reduced graphene oxide (rGO) films have gained significant scientific attention due to their outstanding physicochemical properties, such as large surface area, high conductivity, and chemical stability, along with its low cost and availability.[1,2] These properties make rGO films suitable candidates for use as flexible and transparent electrodes with high capacitance and low sheet resistance[3,4] in energy[5] and healthcare applications,[6,7] among others.

The characteristic structure of this material is strongly influenced by the solution-driven assembly process of the graphene oxide (GO) film, in which stacking of GO flakes from a solution can result in the formation of a free-standing porous film containing micro and nanopores[8] as well as interlayer nanochannels.[9,10] This characteristic structure of the GO film, combined with the necessary reduction process of the GO to rGO, governs the

M. del P. Bernicola, J. Padilla-Pantoja, J. Santiso, J. A. Garrido, E. del Corro
Catalan Institute of Nanoscience and Nanotechnology (ICN2)
CSIC and The Barcelona Institute of Science and Technology
Campus UAB
Bellaterra, Barcelona 08193, Spain
E-mail: joseantonio.garrido@icn2.cat; elena.delcorro@icn2.cat

The ORCID identification number(s) for the author(s) of this article can be found under https://doi.org/10.1002/adfm.202408441

DOI: 10.1002/adfm.202408441

M. Lounasvuori, T. Petit
Young Investigator Group Nanoscale Solid-Liquid Interfaces
Helmholtz-Zentrum Berlin für Materialien und Energie GmbH
Albert-Einstein-Str. 15, 12489 Berlin, Germany

C. Debiemme-Chouvy, H. Perrot
Sorbonne Université, CNRS, Laboratoire Interfaces et Systèmes
Electrochimiques, LISE
UMR 8235, Paris 75005, France

J. A. Garrido
ICREA
Barcelona 08010, Spain

electrochemical performance of the rGO films.[11] Among the several reduction processes discussed in the literature,[12,13] hydrothermal reduction (HT) is considered a simple, fast and environmentally friendly process, which in addition offers the advantage of minimizing the generation of graphene defects due to the low temperatures involved in the process.[14] Importantly, the HT reduction process promotes the evolution of gaseous species, such as H_2O and CO_2, which influences the rGO morphology and porosity.[13,15] HT treatment also results in residual oxygen-containing functional groups decorating the rGO film, thus modifying its hydrophobic nature.[16] Altogether, the HT reduction process significantly impacts on the electrochemical properties of the obtained rGO films.

It is well known that the electrochemical double-layer (EDL) caused by the electrostatic attraction between the polarized electrode and the counter-ions that get adsorbed onto the electrode surface is the origin of its electrochemical capacitance.[17] Recent theoretical research suggests that the dynamics of adsorption within a nanoporous structure differ from those in the bulk due to the confined nature of the electrolyte.[18] For instance, an extraordinary increase in capacitance has been observed, both experimentally[19] and theoretically,[20] when the pore dimension is <1 nm. This deviation from the standard EDL behavior has motivated intensive research. It is suggested that due to the limited ion diffusion into nanocavities,[21,22] ions need to desolvate to enter such small spaces, thus reducing the minimum distance between the ions and the pore walls,[23,24] which has been described as the origin of the enhanced capacitance.[25,26] However, a complete understanding of the structure of nanoporous carbon materials (such as rGO films), the role of confined water, the resulting nano-interfacial phenomena, as well as the ionic transport (especially in the hydrophobic nanochannels),[20,27] are missing, yet being crucial to exploit the electrochemical properties of rGO devices for a number of applications. In this context, advanced in situ/operando characterization techniques are needed to understand nanoconfinement phenomena that accompany the porous nature of rGO and to reveal the origin of the EDL in nanoporous electrodes under working conditions.[28]

In this work, electrodes based on HT rGO films are activated by applying cyclic voltammetry (CV). The voltage-controlled electrochemical activation (EA) results in a drastic enhancement of the electrode electrochemical performance, measured as an increase in the areal capacitance and a decrease in the impedance. By combining different advanced in situ/operando analytical techniques, including electrochemical quartz crystal microbalance (EQCM), X-ray diffraction (XRD), Fourier transform infrared (FTIR), and Raman spectroscopy, we shed light on the chemical and structural changes that boost the electrochemical performance of nanoporous rGO electrodes. This work provides fundamental detailed information about ionic electro-adsorption/desorption and charge transfer processes taking place at the electrode-electrolyte interface in the nanometric cavities of the rGO-based material, which will be key to engineer nanoporous materials and devices for a number of applications.

2. Experimental Section

2.1. Material Fabrication

A graphene oxide solution of 0.15 $mg \cdot mL^{-1}$ was prepared from a commercial GO dispersion of 1w.% composed of graphene flakes of 1 nm thickness (Global Graphene Group). The GO film was prepared by filtering 40 mL of this solution, using an anopore inorganic anodistic membrane (47 mm diameter) with 0.02 µm pore size, for 16 h. Depending on the volume and filtration conditions, the GO film thickness could be controlled. To fabricate the electrodes, from this filtered film, 4 mm GO disks were mechanically prepared, peeled off, and transferred to a gold substrate by a wet transfer method. This standard gold substrate was based on Si/SiO_2 wafers with a layer of Ti/Au (10/100 nm) deposited using an electron beam vapor deposition system. Different substrates were used when required for a specific in situ/operando characterization method. GO films were hydrothermally reduced, using a commercial autoclave, for 3 h at 134 °C and 2 bar. After reduction, the rGO film is encapsulated with polidimetilsiloxano (PDMS) leaving an exposed central region of typically 1.5 mm in diameter. The exposed area can be changed depending on the characterization method used.

2.2. Electrochemical Characterization

A SP-200 Biologic potentiostat was used for the electrochemical characterization using a three-electrode configuration, with rGO, Pt wire and an Ag/AgCl flexible electrode as the working, counter and reference electrodes, respectively. The working solution was phosphate buffer solution (PBS) 150 m (10 mM PBS, 137 mM NaCl and 3 mM KCl) tablets from Sigma–Aldrich diluted in MilliQ water. CV was performed with a scan rate (ν) of 50 $mV \cdot s^{-1}$ in a potential window (ΔV) from −0.9 to 0.8 V versus Ag/AgCl. The capacitance normalized by the geometrical area (C_A) was calculated via integration of CV curves following Equation (1):

$$C_A = \frac{1}{2A\nu\Delta V}\int_{V_1}^{V_2} I(V)\,dV \tag{1}$$

where I is the current response during CV, and A is the geometric area of the electrode exposed to the solution.[29]

Potentiostatic electrochemical impedance spectroscopy (PEIS) was performed at 0.2 V versus Ag/AgCl, with an amplitude of 10 mV and in a frequency range from 10 kHz to 10 mHz. Bode plot representation is used to evaluate the module of the impedance ($|Z|$) and the phase (Z) changes during EA. A PEIS voltage scan was performed modifying the applied potential in steps of 0.2 V, starting from the most positive potential (0.8 V vs Ag/AgCl) to the most negative one (−0.9 V vs Ag/AgCl). The Bode plot was fitted using an equivalent circuit represented in **Figure 1d**, using Zview software. The used model includes a solution resistance (R_s) followed by a circuit element Finite Length Warburg-Open Circuit Terminus (Wo), which is analogous to a wave transmission line for porous materials (more details can be found in the Supporting Information). For the calculation of

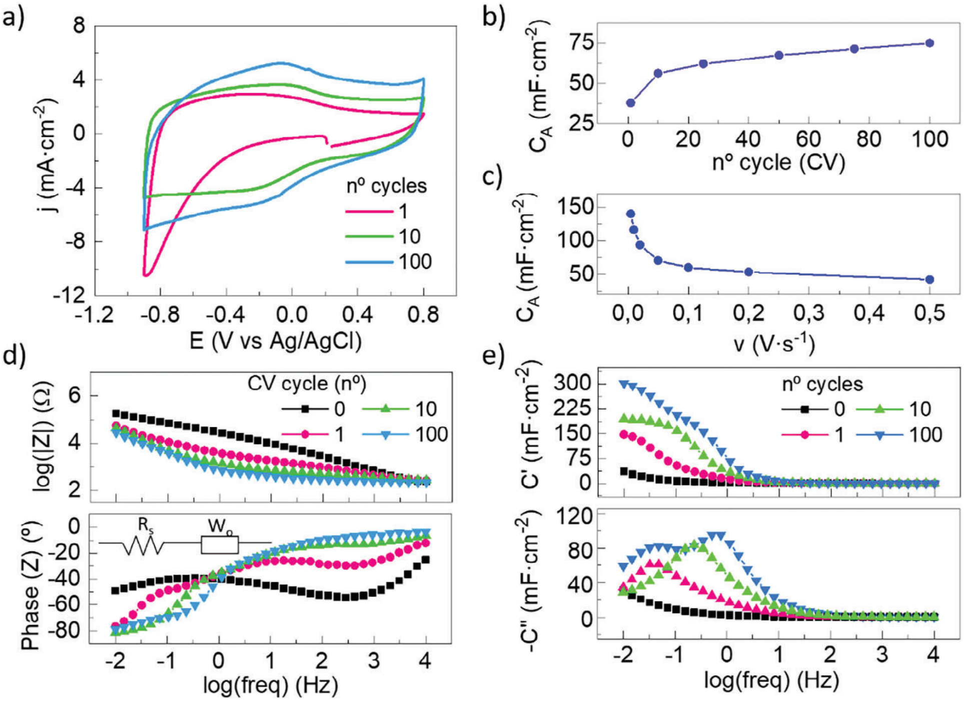

Figure 1. EA of rGO in PBS 150 mм. a) CV activation evolution at different EA time-points (50 mV·s^{-1}). b) C_A evolution as a function of CV cycle number, during EA. c) C_A as a function of the scan rate after EA. d) PEIS measurement, applied potential of 0.2 V versus Ag/AgCl (inset equivalent circuit). e) real (top) and imaginary capacitance (bottom) representation as a function of frequency at different EA time-points.

the complex capacitance, defined by the real capacitance (C') and imaginary capacitance (C''), see Supporting Information.

2.3. In Situ/Operando XRD

XRD measurements were performed in ambient conditions with a Malvern PANanalytical X'Pert Pro diffractometer in reflection geometry, coupled with a ceramic X-ray tube of Cu Kα radiation (λ = 1.540598 Å). The measurements were performed in a 2θ range from 5° to 45°, with a step of 0.03°. A custom-made electrochemical cell was designed to be coupled to the XRD equipment (see Supporting Information for cell design and setup). The interlayer spacing, or d-spacing (d), between flakes was calculated following Bragg's law equation (Equation (2)):

$$\lambda = 2d\sin(\theta) \qquad (2)$$

where λ is 1.540598 Å and θ is the registered diffraction angle.

Operando XRD spectra were recorded with 4 min of acquisition time, at each applied potential, starting from the most positive potential (0.8 V vs Ag/AgCl) to the most negative one (−0.9 V vs Ag/AgCl), and then backward to the initial potential, in steps of 0.2 V. Diffraction peaks were fitted using Gaussian (amplitude) functions, also extracting the peak width as the full width at half maximum (FWHM). The GO diffraction pattern was fitted using a single contribution, for the characteristic peak of the (001) plane at $2\theta \approx 10^{\circ}$,[30] while the rGO diffraction pattern was fitted using two contributions, the peak corresponding to the (002) plane at $2\theta \approx 25^{\circ}$ and an additional peak at $2\theta \approx 18.9^{\circ}$, coming from stacking inhomogeneities due to the presence of remaining oxygenated functional groups.[31]

2.4. In Situ/Operando FTIR

FTIR measurements were performed in the attenuated total reflectance (ATR) mode using a Bruker 70 v spectrometer and a liquid nitrogen-cooled MCT detector. The spectrometer operated under vacuum conditions. A deposition of Ti/Au (4/8 nm) to the ATR crystal based on silicon wafer (Irubis) was used to ensure the conductivity and the rGO adhesion. The spectra were recorded from 4500 to 750 cm^{-1} using a frequency rate of 40 kHz after 1 h in vacuum to remove the humidity. The spectra were referenced to a background spectrum of a bare ATR-Ti/Au substrate. The ATR/rGO was mounted in a custom-built spectroelectrochemical cell externally connected to a potentiostat (SP-200 Biologic). In situ FTIR spectra consisting of 128 scans were recorded at open circuit voltage (OCV) after several CV cycles during EA. Operando FTIR measurements were recorded during the CV cycling. Each spectrum consisted of 14 scans and was recorded with a 4 s waiting time, to obtain a spectrum each 100 mV while CV cycling at 20 mV■s^{-1}.

FTIR absorption characteristic bands are: i) the bands related to water, H—O—H bending mode (δ_{H2O}, ≈1640 cm^{-1}) and O—H stretching mode (ν_{O-H}, ≈3400 cm^{-1}).[32] The ν_{O-H} band was divided into three contributions according to the O—H bonding strength, from weaker to stronger H-bonded (free water ≈3250 cm^{-1}, weakly bonded ≈3450 cm^{-1} and, confined water ≈3600 cm^{-1}).[33,34] ii) the bans related to oxygen functional groups assigned to carbonyl/carboxyl stretching mode ($\nu_{COOH/C=O}$, ≈1749 cm^{-1}) and C—O stretching mode associated to organic intermediates such hydroquinones (ν_{C-O}, ≈1010 cm^{-1}).[35,36] iii) The band related to aromatic C=C stretching mode ($\nu_{C=C}$, ≈1595 cm^{-1}). The area of the $\nu_{COOH/C=O}$ and confined water (ν_{O-H}) peaks were fitted using Gaussian (amplitude) and Lorentzian functions, respectively.

2.5. In Situ/Operando Raman Spectroscopy

Raman spectra were acquired using a Witec spectrograph Alpha300R equipped with a 488 nm excitation laser and a 600 grooves-per-nm grating. A 63x immersion objective was used and the laser power was kept <0.1 mW to prevent sample damage. Samples were prepared using the standard substrates and encapsulation. In situ measurements were performed mapping a 10 × 10 µm area of the rGO electrode, with 1 µm spatial resolution and an integration time of 3 s. Operando measurements were performed using a custom-made electrochemical cell coupled to a Biologic SP-200 potentiostat, using a three-electrode configuration. Real-time spectra of 5 s acquisition time were performed following EA during the overall 100 CV cycles (10 Raman spectra per CV cycle).

Witec PROJECT 5.0 software was used to fit the Raman contributions using Lorentzian fitting functions. The Raman band intensity was calculated as the amplitude of the peak, with exception of Figure 4d, where the intensity was calculated as the area of the peak, in accordance with Eckman et al.[37] Raman spectrum deconvolution includes: i) the characteristic contributions of graphene G (1582 cm^{-1}) and 2D (2700 cm^{-1}) bands,[38] ii) the bands attributed to defects D (1350 cm^{-1}), D' (1625 cm^{-1}) and D+G (2900 cm^{-1}),[38] and iii) the bands correlated with the oxygen content and crystallinity D*(1150–1200 cm^{-1}) and D'' (1500–1550 cm^{-1}).[39]

2.6. EQCM and QCM-D

EQCM measurements were performed with a custom-made quartz crystal microbalance (QCM), coupled to an Autolab potentiostat (PGSTAT12).[40] GO was transferred on a gold electrode over the quartz crystal resonators (9 MHz-AWS, Valencia, Spain), with a surface area of 0.2 cm^2. Before EQCM measurements, the gravimetric regime was assured by measuring the film acoustically, monitoring the QCM dissipation (QCM-D), using an Agilent 429A impedance analyzer (see Supporting Information for more details). The EQCM measurements were performed in a three-electrode configuration by recording the frequency changes with the QCM during the EA, performed at 50 mV·s^{-1}. To provide information about the mass change during EA, the frequency change (Δf_m) of the QCM resonator with respect to the initial frequency value in OCV was converted to mass change (Δm), following Sauerbrey, Equation (3):[41]

$$\Delta m = -k_s \times \Delta f_m \tag{3}$$

where k_s is the theoretical sensitivity factor (experimental factor is 1.09 ng·Hz^{-1} for 9 MHz quartz resonator).

3. Results and Discussion

3.1. Electrode Morphological Characterization

Porous rGO thin films were prepared as explained before, resulting in 1.5 µm thick films, measured by cross-sectional SEM, see Figure S1a (Supporting Information): This image also reveals the rGO characteristic stacked microstructure. The film was analyzed by XRD before and after HT reduction. Figure S1b (Supporting Information) shows the characteristic diffraction peak of GO and rGO films, at 2θ angle of 11.4° and 24.1°, indicating a reduction of the *d*-spacing between flakes, from 7.8 to 3.7 Å, respectively. The chemical composition of GO and rGO films was analyzed using X-ray photoelectron spectroscopy (XPS). Figure S1c (Supporting Information) reveals that upon reduction of the GO film, the C/O ratio increases from 2.5 to 6, corresponding to a higher content of oxygen for GO (≈28%) compared to rGO (≈14%). The evolution of chemical functional groups after the reduction process was analyzed by the deconvolution of C1s peak, revealing that the main effect of the reduction process is associated with the decrease in the C—O/C—OH content, from 25% down to 19%, followed by the C=O group, decreasing from 19% down to 5% (see Figure S1d, Supporting Information).

The porosity nature of rGO is evaluated by nitrogen adsorption–desorption curves (see Figure S2, Supporting Information). The results reveal the presence of pores with an average width <4 nm. Additionally, in transmission electron microscopy, TEM, (Figure S2c, Supporting Information) a nanostructure characteristic of staked 2D materials like GO or rGO is appreciated. Given the nanometric dimensions of the pores, and for the sake of clarity, we will use the term nanoporous graphene.

3.2. Electrochemical Activation of rGO Electrodes

As previously reported for similar carbon-based porous materials,[42,43] an electrochemical process is necessary to activate the rGO electrodes so that they can reach their maximum electrochemical performance. In our case, the EA consists of a series of CV's. Figure 1a shows 1st, 10th, and 100th CV curves during EA of the rGO electrodes, revealing a significant evolution of the voltammogram shape along the EA process, in particular an increase of the current. Figure 1b depicts C_A as a function of the cycle number, showing that it increases with the number of cycles, starting from 38 mF·cm^{-2} and reaching quasi-stationary state at ≈75 mF·cm^{-2}. It is interesting to note that the value of the of rGO is several orders of magnitude higher than that of non-porous graphene electrodes. For instance, the area-normalized double-layer capacitance of single-layer graphene is in the range of 2 µF·cm^{-2}.[44] Such phenomenon is due to high electroactive surface area of rGO that enhances the real C_A. Figure 1c represents C_A as a function of the scan rate; the observed decrease of C_A with increasing ν is characteristic of nanoporous electrodes, and results from the suboptimal use of the available electroactive area due to the more sluggish ion dynamics in the nanopores at high scan rates.[45]

The shape of the CV curves after the EA process (defined after CV cycle number 100) suggests that the rGO electrodes present a characteristic pseudocapacitive behavior,[46] with a deviation from the ideal capacitive response mainly at negative potentials. It is found that in order to reach such pseudocapacitive response, leading to the maximum electrode performance, it is necessary to activate the electrode by means of cycling at negative potentials (see Figure S3a, Supporting Information). We speculate that the negative potential triggers an electrochemical activation mechanism, the origin of which will be discussed in the following. In addition, the CV's reveal two related redox peaks at −0.1 and 0.1 V versus Ag/AgCl which, according to the literature, are attributed to the reversible protonation of remaining oxygenated functional groups.[19] This redox activity thus contributes to the overall electrochemical response of the rGO electrodes.

In order to study changes in the electrical response of the material during EA, PEIS was performed. Figure 1d shows the PEIS of the rGO electrode before and after the 1st, 10th, and 100th CV cycles of the EA process. PEIS is displayed in a Bode plot, which represents the module and phase of the electrochemical impedance, Z, as a function of the frequency. The EA induces a significant drop of the impedance of the rGO electrodes: at low frequency (0.1 Hz) the impedance module decreases from 68.7 to 3.5 kΩ, and at high frequency (1 kHz) it decreases from 665 to 230 Ω. Such impedance decrease is attributed to the increase in the electrochemical active area, which is hypothesized to result from the ingress of the electrolyte solution within the nanoporous electrode (as confirmed by the water uptake studies, see Figure S4, Supporting Information). Additionally, as shown in Figure 1d, the EA process also impacts the phase of the impedance; at low frequency the phase changes from ≈−45° to −90° with the EA. It has been observed that in nanoporous electrodes the phase of the impedance is dominated by diffusion, only reaching values close to −90° when the electrolyte solution ingress in the volumetric electrode is complete and all the pores in the material contribute to the signal.[47]

PEIS data can be fitted using an equivalent electrical circuit (see Figure S5, Supporting Information) governed by a Warburg diffusion element, in particular by an open-ended, finite-length transmission line element, which can be used to model the effect of the electrolyte diffusion in porous electrodes.[47,48] From the analysis of the fitting parameters (see Table S1, Supporting Information), it can be concluded that the diffusion resistance component of the Warburg element, corresponding to the resistance of ionic species to diffuse through the electrode pores,[49] decreases strongly with the number of CV cycles during the EA. Further analysis reveals the decrease of the relaxation time constant of the Warburg element during the EA; being related with the porous length and diffusion coefficient, the decrease of the relaxation time constant suggests a more optimal utilization of the material's porosity as diffusion is increased.

A key performance parameter when considering nanoporous graphene electrodes for applications is the frequency response of the capacitance. To evaluate this, a complex representation of the PEIS is shown in Figure 1e, with the real capacitance (C') and the imaginary capacitance ($-C''$) plotted as a function of frequency, for different cycles during the EA (see Supporting Information for the definition and calculation of the real and imaginary capacitance). It is observed that C' increases with EA (from cycle 1 to 10) and shows a plateau at low frequency. This result is consistent with the hypothesis that EA promotes the electrolyte diffusion into the rGO pores. With further CV cycling (cycle 100th) a second plateau starts to be observed, which we attribute to the existence of additional pores of different (lower) sizes that become accessible to the electrolyte.[50] Figure S3b (Supporting Information) shows the C' as a function of frequency at different applied potentials once the rGO is activated, revealing a potential dependence of the electrode capacitance consistent with the CV experiments which we discuss here below in terms of the pseudocapacitive nature of the rGO electrodes.

3.3. Irreversible Morphological and Chemical Evolution

To gain insight into EA mechanisms we have used advanced in situ and operando characterization tools. EQCM measurements were applied to investigate mass changes in the rGO electrodes during the EA process. To this end, the GO film was transferred on the gold electrode of a quartz crystal resonator, this system allows us to monitor the dynamic response of reactions at the electrode/solution interface (see Experimental Section for additional information about our setup and the mass change calculation). **Figure 2a** shows the mass evolution during the whole EA process, revealing the following phenomena: 1) an irreversible mass increase during the 1st cycle (pink curve), 2) a progressive mass decrease during the next tens of cycles, and 3) a stationary behavior after 50 cycles. Very importantly, a reversible voltage-dependent mass change is observed during the whole EA process.

The observed initial irreversible mass change after the first cycle (inset in Figure 2a) corresponds to a mass increase of ≈0.2 $\mu g \cdot cm^{-2}$, which is attributed to the process of filling the nanopores with the aqueous electrolyte, as previously reported.[51] To monitor this process of water uptake, in situ FTIR measurements were performed during EA. Figure 2b shows in situ FTIR spectra of an rGO electrode recorded before EA and after the 1st, 25th, and 50th CV cycle. The in situ FTIR experiments reveal that, with the increasing number of cycles, there is an increase in the ν_{O-H}, between 3100 and 3600 cm^{-1}, and in the δ_{H-O-H}, which supports the hypothesis of the water uptake induced during the EA. The assignment of the bending and stretching modes related to water were confirmed by conducting the same experiments using an isotopic dilution of deionized H_2O and D_2O (See Figure S7, Supporting Information). It is interesting to note that the FTIR peak mainly contributing to the observed ν_{O-H} increase in intensity is the one attributed to confined water.

FTIR reveals that the water uptake process occurs during the whole EA process, although in EQCM measurements this phenomenon is only observed in the 1st cycle, as a clear mass increase. From the 2nd cycle onward the EQCM reveals a progressive mass loss indicating an additional phenomenon along with the water uptake process. From the FTIR data, it can be concluded that the electrochemical process induces further chemical reduction of the rGO film,[52] which can explain the progressive mass decrease observed in the EQCM experiment. During EA, a reduction of $\nu_{C=O}$ is observed, along with an increase of the aromatic $\nu_{C=C}$.[35] Moreover, there is a slight increase of the ν_{O-C} band which suggests the formation of organic intermediates such as lactones and hydroquinones during the reduction process.[36]

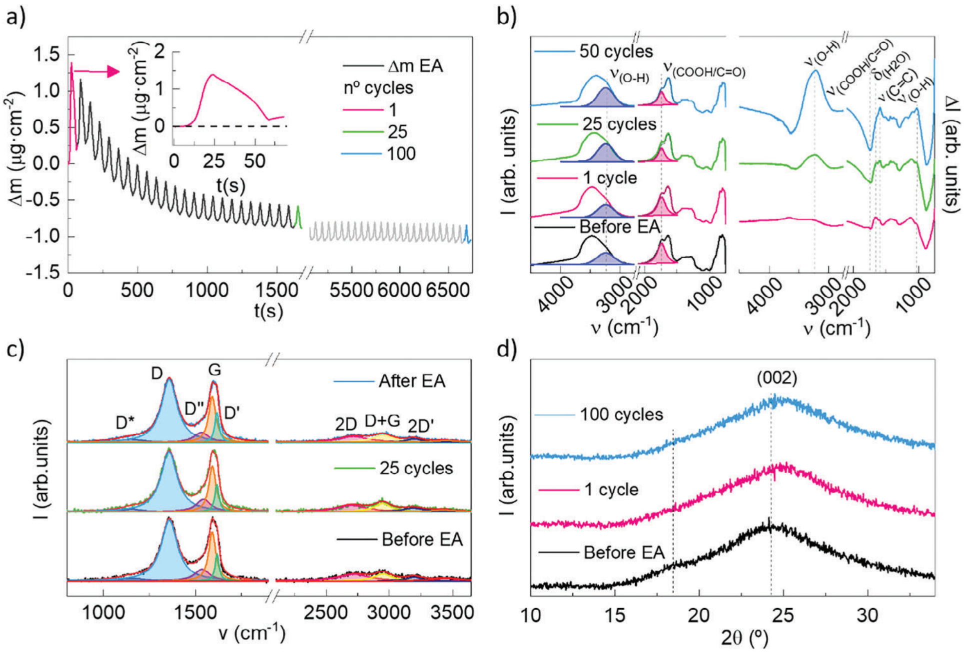

Figure 2. In situ/operando characterization at different EA time-points of activation, in PBS 150 mM. a) Mass evolution, calculated from the frequency change of EQCM (inset first cycle). b) FTIR spectra (left) and difference spectra, referenced to spectrum before EA (right). FTIR spectra fitting curves, including $\nu_{C=O}$ Lorentzian and ν_{O-H} strong Gaussian fitting functions. c) Raman spectra and Lorentzian fitting functions (see Experimental Section). d) XRD patterns.

In situ Raman spectroscopy can also provide complementary information on the impact of the reduction process on the properties of the rGO film.[38] Figure 2c shows in situ Raman spectra at different time-points during activation: the 0th, 25th, and 50th CV cycle. A narrowing of the so-called D band during the initial CV cycles of the EA is observed, as a clear indicator of material reduction.[53] Additionally, a decrease in the intensity ratio I_{D+G}/I_D is observed. This parameter is typically associated with a decrease in the graphene resistivity due to the rGO reduction,[54] and is in good agreement with our PEIS results. The evolution of the different Raman parameters is presented in Table S3 (Supporting Information).

The chemical reduction of the nanoporous rGO film induced by the EA is expected to influence the structural properties of the film, which are investigated by in situ XRD. Figure 2d depicts the XRD patterns obtained at different times during the EA process, the 0th, 1st, and 50th CV cycle, showing the characteristic diffraction peak (002) associated with the distance between the rGO flakes.[55] It is observed that EA induces an irreversible shift of the (002) peak toward larger 2θ angles, thus implying a lowering of the d-spacing with EA, from 3.66 Å down to 3.5 Å. This lowering of the d-spacing is consistent with the removal of oxygen-containing functional groups, which have a marked out-of-plane structure.[56] Not only the position of the (002) peak changes with EA, but also its FWHM, which decreases from 8.7 down to 8.1, in good agreement with previous observations, indicating a transition toward a film with a more homogeneous stacking of the rGO flakes due to the removal of oxygen groups.[10] The decrease of the d-spacing has an effect on the rGO film thickness. In Figure S8 (Supporting Information), SEM cross-section images of the rGO are presented before and after EA, revealing a thickness decrease.

In light of the above results, a strong connection between the reduction process and the increase of the electrode capacitance is found, as summarized in **Figure 3**, where the electrode mass change and capacitance are plotted together as a function of the cycle number during EA.

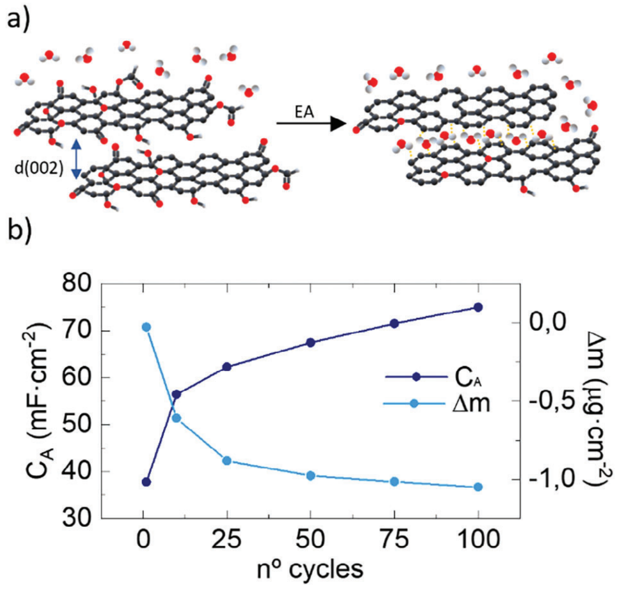

Figure 3. a) Schematic representation of the irreversible phenomena taking place during the EA, including chemical reduction process, d-spacinsg decrease, and water confinement. b) C_A, calculated from CV, and Δm, obtained from the EQCM experiments, as a function of CV cycle number.

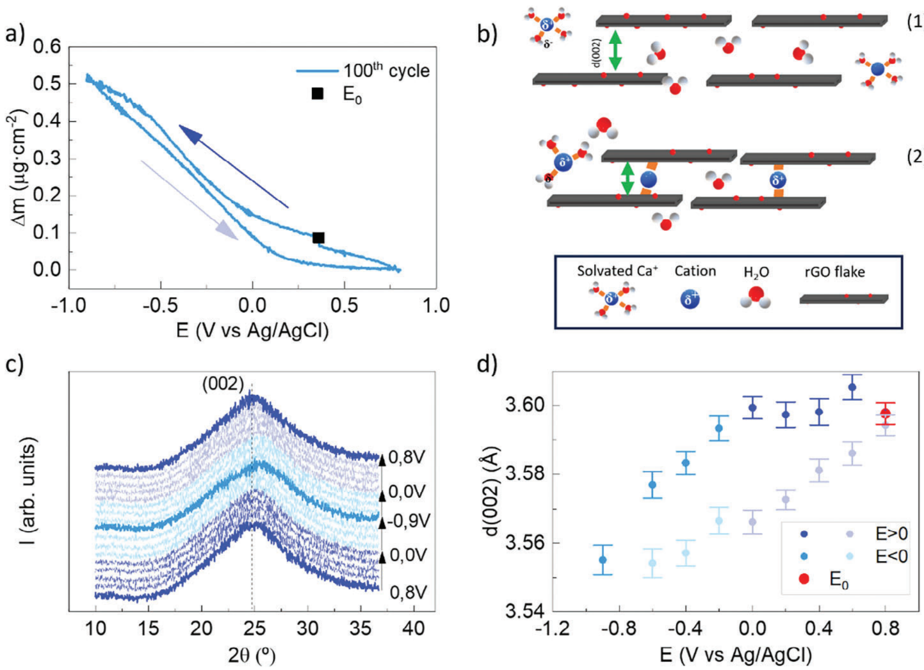

Figure 4. Operando characterization after EA, in PBS 150 mм. a) Δ*m* with bias during a CV (50 mV·s^{-1}). b) Schematic representation of the reversible phenomena after EA, including cation electro-adsorption/desorption process and *d*-spacing modulation. c) (In situ) XRD patterns measured at different applied potential during a simulated CV. d) *d*-spacing (*d*(002)) as a function of applied potential, calculated from the maximum of the (002) peak, in Figure 4c, using Bragg's equation (datum in red indicates the initial potential of the simulated CV).

The formation of intermediate hydroquinones during electrochemical reduction results in an increase of the electrode capacitance. In addition, the reduction process, especially this taking place at the edges of the GO flakes, modifies the functionality and wettability of the pores in the rGO film. This change enhances the hydrophilicity of the nanochannels[57] which, in turns, improves the diffusion process. To assess this possibility, contact angle measurements (see Figure S9, Supporting Information) were conducted, confirming that after EA the rGO films exhibited a more hydrophilic nature, which is consistent with an enhanced wettability after reduction, facilitating the ingress of water of confined nature in the nanochannels.[58]

3.4. Dynamics at the Nanoporous rGO Electrode/Electrolyte Interface

Along with the EA process, we also observed reversible electrochemical phenomena related to the pseudocapacitive behavior of the electrode. A known mechanism contributing to the pseudocapacitance, already observed in the CV measurements, is the protonation/deprotonation of remaining oxygenated groups in the rGO electrodes.[19] To confirm this reversible redox reaction, operando FTIR was performed by controlling the electrochemical potential at the electrode/electrolyte interface during FTIR spectra acquisition. While cycling to negative polarization, a reversible intensity decrease in the $\nu_{C=O/COOH}$ band is observed, along with an increase in the stretching mode of the carboxylate peaks (asymmetric mode ν_{COO-} at 1584 cm^{-1} and symmetric mode ν_{COO-} at 1430 cm^{-1}),[36] see Figure S10 (Supporting Information) for a more detailed description.

A further hint on the origin of the pseudocapacitive behavior is offered by the EQCM experiments depicted in Figure 2a, which reveal a reversible polarization-dependent mass modulation that occurs during and after the EA process. **Figure 4a** depicts the EQCM mass evolution after the EA. This experiment shows a reversible variation of the electrode mass at negative polarization, of ≈±0.5 μg·cm^{-2}, and an almost negligible mass change at positive polarization. This observation is tentatively attributed to a reversible electro-adsorption/desorption process dominated by cationic species of the solution, as sketched in Figure 4a, which enhances the electrode charge storage capability.[59] To confirm this hypothesis, operando XRD and Raman experiments were conducted.

Figure 4c depicts XRD spectra registered at applied potential from 0.8 to −0.9 V, and back to 0.8 V, in 0.2 V steps. Figure 4d shows the rGO *d*-spacing (*d*(002) in the figure) as a function of the applied potential. While *d*(002) does not change significantly during positive polarization, it does decrease when negative polarization is applied, returning to the initial value once the bias is swept back. This reversible potential dependence of the *d*-spacing is consistent with the electrostatic adsorption of cations at negative polarization, which leads to an enhanced staking of the rGO flakes (lowering the *d*-spacing).[60] Operando FTIR experiments complement this cation electro-adsorption process observation (see Figure S10, Supporting Information). The intensity of the ν_{O-H} band at 3630 cm^{-1}, corresponding to free water, increases due to the desolvation process of the cationic species as they get adsorbed.

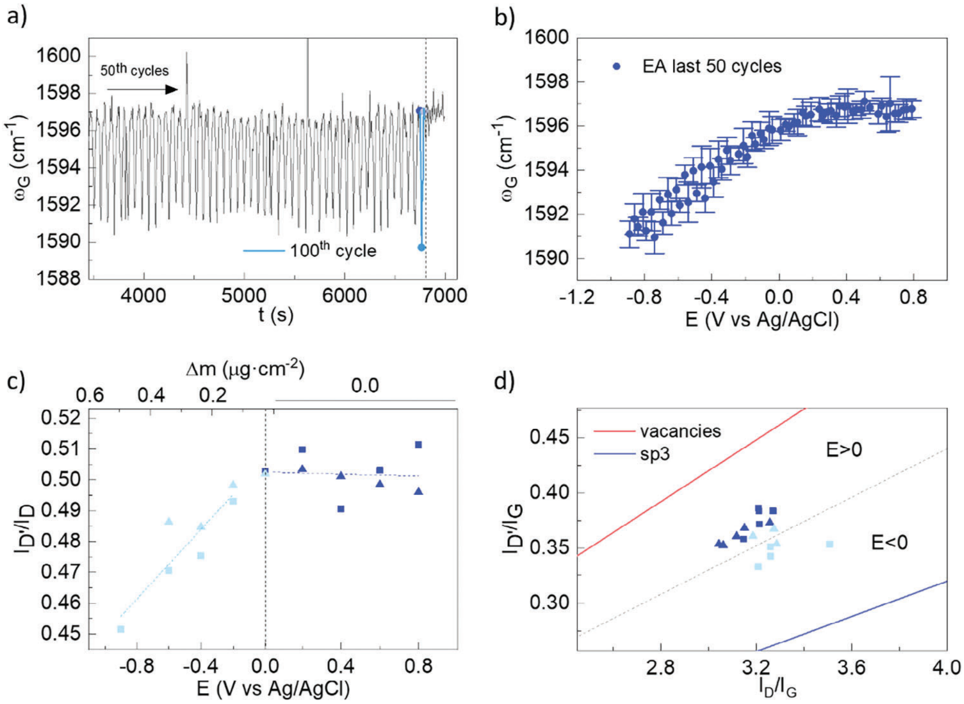

Figure 5. Operando Raman spectroscopy, in PBS 150 mм. a) Time scan of ω_G for the last 50 CV cycles during EA (50 mV·s^{-1}). b) Average ω_G (from Figure 5a) as a function of applied potential. c) Intensity ratio $I_{D'}/I_D$ as a function of applied potential after EA. d) Intensity ratio $I_{D'}/I_G$ as a function of intensity ratio I_D/I_G after EA. Linear functions corresponding to vacancies (red) and sp^3 (blue) defects, according to Ref.[37]. In c) and d) different symbols (squares and triangles) stand for the different CV scan directions. Dashed lines are guides to the eye.

Using operando Raman spectroscopy, in which the energy of the G band can be used to monitor charge modulation in graphene materials,[53] the polarization dynamics of the rGO electrodes were investigated. **Figure 5a** shows the time scan of the G band frequency (ω_G) during multiple polarization cycles after EA, revealing a reversible modulation of ω_G with the applied potential. Figure 5b depicts the average potential-dependent modulation of ω_G for the rGO electrode after EA, in good agreement with the observed potential dependence of the mass evolution shown in Figure 2a. While ω_G remains almost constant under positive polarization, it downshifts with negative polarization, shifting by ≈6 cm^{-1} at the most negative bias. It is suggested that the polarization-induced cation electro-adsorption leads to a weakening of the C─C bonds in rGO, which then results in the observed ω_G downshift.

To further explore the cation electro-adsorption phenomenon, the bias dependence of the defect-related Raman bands (D and D´) was analyzed. The intensity of both bands is related to the density of defects and the lattice disorder of graphene. Furthermore, the intensity ratio between them, $I_{D'}/I_D$, slightly varies depending on the type of defect (vacancies, sp^3 and boundaries).[37] Figure 5c depicts the intensity ratio $I_{D'}/I_D$ of the rGO electrode after EA as a function of the applied potential (bottom axis) and the mass variation calculated from EQCM experiments (top axis). It can be observed that $I_{D'}/I_D$ remains relatively unaltered at positive potential and decreases significantly when negative potential is applied. These results indicate that when a negative potential is applied to the nanoporous rGO electrode, the type of defects in the graphene lattice evolves; furthermore, this defect evolution is reversible. To elucidate the kind of defects and their polarization dependence, Figure 5d presents the intensity ratio $I_{D'}/I_G$ as a function of the intensity ratio I_D/I_G, following the presentation by Eckman et al. Linear functions with different slope are plotted, corresponding to vacancies ($I_{D'}/I_D \approx 0.14$, in red) and sp^3 ($I_{D'}/I_D \approx 0.08$, in blue) defects.[37] During positive polarization, it is observed that $I_{D'}/I_D$ is larger (darker blue data closer to the red line), indicating larger amount of vacancy-type defects. Meanwhile, when negative polarization is applied $I_{D'}/I_D$ decreases (lighter blue data closer to the blue line) indicating an evolution of the defect type toward sp^3. The presence of sp^3 defects during negative polarization, when cationic electro-adsorption occurs, suggests an electrostatic interaction between the adsorbed cations and the electron-rich pi system of the vacancies in the graphene basal plane.

4. Conclusion

In this work, porous electrodes based on rGO are activated following an electrochemical protocol enhancing their electrochemical performance. The electrochemical activation results in an increase of the areal capacitance and of the pseudocapacitive response of the electrode. PEIS characterization concludes that the EA of the rGO-based electrodes promotes ionic diffusion, allowing the electrolyte to reach the smaller, nanometric, cavities of the nanoporous carbon material, leading to an enhancement of the electroactive area and thus an increase of the electrode areal capacitance. The combination of advanced in situ/operando characterization tools reveal that during the EA there is a further irreversible reduction of rGO-based electrode. The reduction of the residual oxygenated groups of the nanopores decreases the *d*-spacing between the rGO flakes and changes the hydrophobicity of such small cavities, which impacts the ionic diffusion process, boosting the areal capacitance of the electrode.

Once activated, the electrodes exhibit a polarization dependent dynamic response. EQCM reveals a reversible mass modulation at negative potential, attributed to the electro-adsorption/desorption process of cationic species. This cation adsorption is also reflected in a reversible modulation of the *d*-spacing obtained by XRD. The adsorption of positive ions favors the inter-flake stacking due to the electrostatic interaction between the cation and the carbon lattice. Given the small dimensions of the rGO pores, the cations must de-solvate to diffuse into the pores, as indicated by the operando FTIR results. The cationic adsorption event is further explored with operando Raman spectroscopy. A reversible evolution of the nature of the rGO defects, from vacancies to sp^3, confirms the electrostatic interaction between cations and the graphene basal plane. By using in situ/operando analytical techniques, this study helps to elucidate the complex interplay between surface chemistry, ion confinement, and desolvation processes occurring during electrochemical cycling of rGO-based electrodes. This fundamental knowledge is key to engineer nanoporous graphene-based electrodes with enhanced electrochemical performance for a number of applications.

Supporting Information

Supporting Information is available from the Wiley Online Library or from the author.

Acknowledgements

Part of the present work has been performed in the framework of Universitat Autònoma de Barcelona Materials Science PhD programme; This work has received funding from the European Union's Horizon 2020 research and innovation programme under grant agreement N° 825213 (WASP); the European Union's Horizon 2020 research and innovation programme under grant agreement N° 881603 (GrapheneCore3); the European Union's Horizon 2020 research and innovation programme under grant agreement N° 101070865 (MINIGRAPH); and MCIN/ AEI /10.13039/501100011033 under grant agreement PID2020-113663RB-I00. E.d.C. acknowledges the RYC2019-027879-I Grant funded by MCIN/AEI/10.13039/501100011033.

Conflict of Interest

J.A.G. declares that he holds interest in INBRAIN Neuroelectronics which has licensed technology described in this paper. All other authors declare no competing interests.

Author Contributions

M.d.P.B. conducted all experiments, analyzed the data, and wrote the original draft; J.P.P. and J.S. contributed to the conceptualization and development of the XRD electrochemical cell; H.P. and C.D.C contributed to the EQCM experiments; M.L. and T.P. contributed to the FTIR studies; J.A. G. and E.d.C. contributed to the design of the study and led its supervision; all authors contributed to the preparation and editing of the manuscript.

Data Availability Statement

The data that support the findings of this study are available from the corresponding author upon reasonable request.

Keywords

cation electro-adsorption, electrochemical activation, nanoporous graphene, operando characterization, pseudocapacitance

Received: May 16, 2024
Published online: June 14, 2024

---

[1] D.-W. Wang, F. Li, M. Liu, G. Q. Lu, H.-M. Cheng, *Angew. Chem., Int. Ed.* **2008**, *47*, 373.
[2] E. T. Mombeshora, E. Muchuweni, *RSC Adv.* **2023**, *13*, 17633.
[3] G. D.e Arco, L. Zhang, Y. Schlenker, C. W. Ryu, K. Thompson, M. E. Zhou, *ACS Nano.* **2010**, *4*, 2865.
[4] C. Lee, X. Wei, J. W. Kysar, J. Hone, *Science.* **2008**, *321*, 385.
[5] A. C. Forse, C. Merlet, J. M. Griffin, C. P. Grey, *J. Am. Chem. Soc.* **2016**, *138*, 5731.
[6] N. V. Apollo, M. I. Maturana, W. Tong, D. A. X. Nayagam, M. N. Shivdasani, J. Foroughi, G. G. Wallace, S. Prawer, M. R. Ibbotson, D. J. S. Garrett, *Adv. Funct. Mater.* **2015**, *25*, 3551.
[7] D. Viana, S. T. Walston, E. Masvidal-Codina, X. Illa, B. Rodríguez-Meana, J. Del Valle, A. Hayward, A. Dodd, T. Loret, E. Prats-Alfonso, N. De La Oliva, M. Palma, E. Del Corro, M. Del Pilar Bernicola, E. Rodríguez-Lucas, T. Gener, J. M. De La Cruz, M. Torres-Miranda, F. T. Duvan, N. Ria, J. Sperling, S. Martí-Sánchez, M. C. Spadaro, C. Hébert, S. Savage, J. Arbiol, A. Guimerà-Brunet, M. V. Puig, B. Yvert, X. Navarro, et al., *Nat. Nanotechnol.* **2024**, *19*, 514.
[8] W.-H. Zhang, M.-J. Yin, Q. Zhao, C.-G. Jin, N. Wang, S. Ji, C. L. Ritt, M. Elimelech, Q.-F. An, *Nat. Nanotechnol.* **2021**, *16*, 337.
[9] K. Guan, Y. Jia, Y. Lin, S. Wang, H. Matsuyama, *Nano Lett.* **2021**, *21*, 3495.
[10] Y. Cao, Z. Xiong, F. Xia, G. V. Franks, L. Zu, X. Wang, Y. Hora, S. Mudie, Z. He, L. Qu, Y. Xing, D. Li, *Adv. Funct. Mater.* **2022**, *32*, 2201535.
[11] L. Baptista-Pires, A. De La Escosura-Muñiz, M. Balsells, J. C. Zuaznabar-Gardona, A. Merkoçi, *Electrochem. Commun.* **2019**, *98*, 6.
[12] C.-H. Chuang, Y.-F. Wang, Y.-C. Shao, Y.-C. Yeh, D.-Y. Wang, C.-W. Chen, J. W. Chiou, S. C. Ray, W. F. Pong, L. Zhang, J. F. Zhu, J. H. Guo, *Sci. Rep.* **2014**, *4*, 4525.
[13] Z. Niu, J. Chen, H. H. Hng, J. Ma, X. Chen, *Adv. Mater.* **2012**, *24*, 4144.
[14] A. Bagri, C. Mattevi, M. Acik, Y. J. Chabal, M. Chhowalla, V. B. Shenoy, *Nat. Chem.* **2010**, *2*, 581.
[15] L. Daoquing, L. Qianwei, Z. Huazhang, *J. Mater. Chem. A.* **2018**, *6*, 11471.
[16] F. T. Johra, W.-G. Jung, *Appl. Surf. Sci.* **2015**, *357*, 1911.
[17] N. Quintanal, D. Barreda, C. Blanco, Z. González, P. Álvarez, M. Granda, M. Sevilla, R. Santamaría, *J. Electrochem. Soc.* **2023**, *170*, 040528.
[18] J. Xiao, H. Zhan, X. Wang, Z.-Q. Xu, Z. Xiong, K. Zhang, G. P. Simon, J. Z. Liu, D. Li, *Nat. Nanotechnol.* **2020**, *15*, 683.
[19] J. Chmiola, G. Yushin, Y. Gogotsi, C. Portet, P. Simon, P. L. Taberna, *Science.* **2006**, *313*, 1760.
[20] C. Merlet, B. Rotenberg, P. A. Madden, P.-L. Taberna, P. Simon, Y. Gogotsi, M. Salanne, *Nat. Mater.* **2012**, *11*, 306.
[21] J. Kang, Y. Ko, J. P. Kim, J. Y. Kim, J. Kim, O. Kwon, K. C. Kim, D. W. Kim, *Nat. Commun.* **2023**, *14*, 901.
[22] T. Mouterde, A. Keerthi, A. R. Poggioli, S. A. Dar, A. Siria, A. K. Geim, L. Bocquet, B. Radha, *Nature.* **2019**, *567*, 87.

[23] J. Chmiola, C. Largeot, P.-L. Taberna, P. Simon, Y. Gogotsi, *Angew. Chem., Int. Ed.* **2008**, *47*, 3392.

[24] W. Sparreboom, A. Van Den Berg, J. C. T. Eijkel, *Nat. Nanotechnol.* **2009**, *4*, 713.

[25] S. Fleischmann, Y. Zhang, X. Wang, P. T. Cummings, J. Wu, P. Simon, Y. Gogotsi, V. Presser, V. Augustyn, *Nat. Energy.* **2022**, *7*, 222.

[26] K. Ge, H. Shao, E. Raymundo-Piñero, P.-L. Taberna, P. Simon, *Nat. Commun.* **2024**, *15*, 1935.

[27] E. Pomerantseva, F. Bonaccorso, X. Feng, Y. Cui, Y. E. S. Gogotsi, *Science.* **2019**, *366*, eaan8285.

[28] A. Venugopal, R. Kas, K. Hau, W. A. Smith, *J. Am. Chem. Soc.* **2021**, *143*, 18581.

[29] E. Zhang, Y.-C. Wu, H. Shao, V. Klimavicius, H. Zhang, P.-L. Taberna, J. Grothe, G. Buntkowsky, F. Xu, P. Simon, S. Kaskel, *J. Am. Chem. Soc.* **2022**, *144*, 14217.

[30] S. Zainab, M. Azeem, S. U. Awan, S. Rizwan, N. Iqbal, J. Rashid, *Sci. Rep.* **2023**, *13*, 6954.

[31] B. Gupta, N. Kumar, K. Panda, V. Kanan, S. Joshi, I. Visoly-Fisher, *Sci. Rep.* **2017**, *7*, 45030.

[32] M. Lounasvuori, Y. Sun, T. S. Mathis, L. Puskar, U. Schade, D.-E. Jiang, Y. Gogotsi, T. Petit, *Nat. Commun.* **2023**, *14*, 1322.

[33] A. W. Knight, N. G. Kalugin, E. Coker, A. G. Ilgen, *Sci. Rep.* **2019**, *9*, 8246.

[34] M. Lounasvuori, T. S. Mathis, Y. Gogotsi, T. Petit, *J. Phys. Chem. Lett.* **2023**, *14*, 1578.

[35] A. Vizintin, J. Bitenc, A. Kopač Lautar, K. Pirnat, J. Grdadolnik, J. Stare, A. Randon-Vitanova, R. Dominko, *Nat. Commun.* **2018**, *9*, 661.

[36] I. O. Faniyi, O. Fasakin, B. Olofinjana, A. S. Adekunle, T. V. Oluwasusi, M. A. Eleruja, E. O. B. Ajayi, *SN Appl Sci.* **2019**, *1*, 1181.

[37] A. Eckmann, A. Felten, A. Mishchenko, L. Britnell, R. Krupke, K. S. Novoselov, C. Casiraghi, *Nano Lett.* **2012**, *12*, 3925.

[38] D. López-Díaz, López Holgado, J. L. García-Fierro, M. M. Velázquez, *J. Phys. Chem. C.* **2017**, *121*, 20489.

[39] D. Radziuk, H. Möhwald, *Phys. Chem. Chem. Phys.* **2016**, *18*, 21.

[40] A. Bouzina, H. Perrot, C. Debiemme-Chouvy, O. Sel, *ACS Appl. Energy Mater.* **2022**, *5*, 14934.

[41] F. Razzaghi, C. Debiemme-Chouvy, F. Pillier, H. Perrot, O. Sel, *Phys. Chem. Chem. Phys.* **2015**, *17*, 14773.

[42] G. Dong, M. Fang, H. Wang, S. Yip, H.-Y. Cheung, F. Wang, C.-Y. Wong, S. T. Chu, J. C. Ho, *J. Mater. Chem. A.* **2015**, *3*, 13080.

[43] D. R. Chen, P. K. Adusei, M. Chitranshi, Y. Fang, K. Johnson, M. Schulz, V. Shanov, *Appl. Surf. Sci.* **2021**, *541*, 148448.

[44] J. Xia, F. Chen, J. Li, N. Tao, *Nat. Nanotechnol.* **2009**, *4*, 505.

[45] H.-J. Liu, J. Wang, C.-X. Wang, Y.-Y. Xia, *Adv. Energy Mater.* **2011**, *1*, 1101.

[46] S. Fleischmann, J. B. Mitchell, R. Wang, C. Zhan, D. Jiang, V. Presser, V. Augustyn, *Chem. Rev.* **2020**, *120*, 6738.

[47] J. Huang, *J. Electrochem. Soc.* **2020**, *167*, 166503.

[48] S. Cruz-Manzo, P. Greenwood, *J. Energy Storage.* **2022**, *55*, 105529.

[49] L. Suárez, V. Barranco, T. A. Centeno, *J. Colloid Interface Sci.* **2021**, *588*, 705.

[50] P. L. Taberna, P. Simon, J. F. Fauvarque, *J. Electrochem. Soc.* **2003**, *150*, A292.

[51] M. D. Levi, G. Salitra, N. Levy, D. Aurbach, J. Maier, *Nat. Mater.* **2009**, *8*, 872.

[52] H. Goubaa, F. Escobar-Teran, I. Ressam, W. Gao, A. El Kadib, I. T. Lucas, M. Raihane, M. Lahcini, H. Perrot, O. Sel, *J. Phys. Chem. C.* **2017**, *121*, 9370.

[53] R. Yadav, P. Joshi, M. Hara, M. Yoshimura, *Phys. Chem. Chem. Phys.* **2021**, *23*, 11789.

[54] X. Díez-Betriu, S. Álvarez-García, C. Botas, P. Álvarez, J. Sánchez-Marcos, C. Prieto, R. Menéndez, A. De Andrés, *J. Mater. Chem. C.* **2013**, *1*, 6905.

[55] K. H. Thebo, X. Qian, Q. Zhang, L. Chen, H.-M. Cheng, W. Ren, *Nat. Commun.* **2018**, *9*, 1486.

[56] S. Pei, J. Zhao, J. Du, W. Ren, H.-M. Cheng, *Carbon.* **2010**, *48*, 4466.

[57] S. D. Bernardina, E. Paineau, J.-B. Brubach, P. Judeinstein, S. Rouzière, P. Launois, P. Roy, *J. Am. Chem. Soc.* **2016**, *138*, 10437.

[58] M. Acik, C. Mattevi, C. Gong, G. Lee, K. Cho, M. Chhowalla, Y. J. Chabal, *ACS Nano.* **2010**, *4*, 5861.

[59] V. Maurel, K. Brousse, T. S. Mathis, A. Perju, P.-L. Taberna, P. Simon, A. C. Operando, *J. Electrochem. Soc.* **2022**, *169*, 120510.

[60] K. Guan, Y. Guo, Z. Li, Y. Jia, Q. Shen, K. Nakagawa, T. Yoshioka, G. Liu, W. Jin, H. Matsuyama, *Nat. Commun.* **2023**, *14*, 1016.